




Volume 62B, No. 12, December 2007

ISSN 0584-8547

# SPECTROCHIMICA ACTA

PART B: ATOMIC SPECTROSCOPY  
Including Spectrochimica Acta Reviews

<p><b>Spectrochimica Acta Part B</b></p> <p><i>Editors</i> <b>M.T.C. DE LOOS</b> <i>Delft</i></p> <p><b>N. OMENETTO</b> <i>Gainesville, FL</i></p> <p><b>Spectrochimica Acta Reviews</b></p> <p><i>Editors</i> <b>A. BOGAERTS</b> <i>Wiley, Antwerp</i></p> <p><b>J.-M. MERMET</b> <i>Tramoyes</i></p> <p><b>R.E. STURGEON</b> <i>Ottawa</i></p>	<p><b>SPECIAL ISSUE</b></p> <p>A COLLECTION OF PAPERS PRESENTED AT THE</p> <p><b>4<sup>TH</sup> INTERNATIONAL CONFERENCE ON LASER INDUCED PLASMA SPECTROSCOPY AND APPLICATIONS (LIBS 2006)</b></p> <p><b>Montreal, Canada</b></p> <p><b>5 – 8 September 2006</b></p> <p><i>Guest Editors:</i> <b>M. Sabsabi</b> <b>R.E. Russo</b></p>
--	---

Available online at  
 **ScienceDirect**  
www.sciencedirect.com

This article was published in an Elsevier journal. The attached copy is furnished to the author for non-commercial research and education use, including for instruction at the author's institution, sharing with colleagues and providing to institution administration.

Other uses, including reproduction and distribution, or selling or licensing copies, or posting to personal, institutional or third party websites are prohibited.

In most cases authors are permitted to post their version of the article (e.g. in Word or Tex form) to their personal website or institutional repository. Authors requiring further information regarding Elsevier's archiving and manuscript policies are encouraged to visit:

<http://www.elsevier.com/copyright>



# Laser-induced breakdown spectroscopy at a water/gas interface: A study of bath gas-dependent molecular species<sup>☆</sup>

M. Adamson, A. Padmanabhan, G.J. Godfrey, S.J. Rehse<sup>\*</sup>

*Department of Physics and Astronomy, Wayne State University, Detroit, MI 48201, United States*

Received 21 November 2006; accepted 12 October 2007

Available online 23 October 2007

## Abstract

Single-pulse laser-induced breakdown spectroscopy has been performed on the surface of a bulk water sample in an air, argon, and nitrogen gas environment to investigate emissions from hydrogen-containing molecules. A microplasma was formed at the gas/liquid interface by focusing a Nd:YAG laser beam operating at 1064 nm onto the surface of an ultra-pure water sample. A broadband Echelle spectrometer with a time-gated intensified charge-coupled device was used to analyze the plasma at various delay times (1.0–40.0  $\mu$ s) and for incident laser pulse energies ranging from 20–200 mJ. In this configuration, the dominant atomic spectral features at short delay times are the hydrogen H-alpha and H-beta emission lines at 656 and 486 nm, respectively, as well as emissions from atomic oxygen liberated from the water and air and nitrogen emission lines from the air bath gas. For delay times exceeding approximately 8  $\mu$ s the emission from molecular species (particularly OH and NH) created after the ablation process dominates the spectrum. Molecular emissions are found to be much less sensitive to variations in pulse energy and exhibit a temporal decay an order of magnitude slower than the atomic emission. The dependence of both atomic hydrogen and OH emission on the bath gas above the surface of the water was studied by performing the experiment at standard pressure in an atmospheric purge box. Electron densities calculated from the Stark broadening of the H-beta and H-gamma lines and plasma excitation temperatures calculated from the ratio of H-beta to H-gamma emission were measured for ablation in the three bath gases.

© 2007 Elsevier B.V. All rights reserved.

**Keywords:** Laser-induced breakdown spectroscopy; LIBS; Molecular spectroscopy; Analysis of water; Echelle spectrometer; Bath gas

## 1. Introduction

The use of laser-induced breakdown spectroscopy (LIBS) as a rapid and convenient technique for the determination of elemental concentration in a variety of samples, including liquids, has been described extensively [1–4]. The difficulties in performing LIBS on or in transparent liquid samples are well-known and include a high breakdown threshold, rapid quenching of the emission, low emission intensity (compared to metal samples ablated in air), splashing and contamination of

nearby optics, and irreproducible spectra due to sample geometry and liquid surface disturbances. Yet the ability to rapidly determine trace contaminant concentrations (particularly dissolved inorganic elements) in a liquid medium (most often water or oil) with LIBS has led many to investigate this powerful tool. To overcome the difficulties inherent in performing LIBS on or in liquid samples, numerous experimental arrangements have been utilized to provide reproducible spectra with high signal-to-noise as is seen during ablation on solid samples. These include ablation on the surface of laminar jets [5–8], ablation in bulk liquids [9–11], ablation on the surface of bulk liquids [12,13], ablation in aerosol mists created by nebulizers [14], double-pulse ablation [15–17], crossed beam ablation [18], ablation in cavitation bubbles [19], ablation on solids placed in the bulk liquids [20], ablation of substrates used to filter the liquid [21,22], all fiber delivery and collection [23], and post-light detection signal processing [24].

The most flexible and convenient use of the LIBS technology involves ablation on the surface of any body of

<sup>☆</sup> This paper was presented at the 4th International Conference on Laser Induced Plasma Spectroscopy and Applications (LIBS 2006) held in Montreal, Canada, 5–8 September 2006, and is published in the Special Issue of Spectrochimica Acta Part B, dedicated to that conference.

<sup>\*</sup> Corresponding author. WSU, Department of Physics and Astronomy, 666 W. Hancock, Detroit, MI 48201. Tel.: +1 313 577 2411; fax: +1 313 577 3932.

E-mail addresses: somarian02@yahoo.com (M. Adamson), sargi5@yahoo.com (A. Padmanabhan), gjgodfre@wayne.edu (G.J. Godfrey), rehse@wayne.edu (S.J. Rehse).

standing liquid — where no additional sample-preparation (e.g. with a jet or a nebulizer) is required. For this type of spectroscopy, the speed and resolution offered by the use of a broadband Echelle spectrometer for the observation of almost all the analyte and matrix emission lines would greatly assist in the applicability of the technique to real-world applications. To this end, the use of Echelle spectrometers for LIBS on both solids and liquids has recently been reported [25–27].

Broadband, single-pulse “panoramic” spectroscopy on the surface of water utilizing an Echelle spectrometer with a variety of pulse energies and delay times has also been studied previously [28]. In this configuration, the dominant atomic spectral features at short delay times were the hydrogen H-alpha ( $H_{\alpha}$ ) and H-beta ( $H_{\beta}$ ) emission lines at 656 and 486 nm, respectively. When LIBS is performed in an air atmosphere, however, the strength of these atomic emissions decreases rapidly with time. At approximately 8  $\mu$ s after the ablation pulse the emission from molecular species created during and after the ablation process by recombination of liberated neutral atoms dominates the spectrum. Specifically for water ablated in air, the dominant spectral features include the  $A^2\Sigma^+ - X^2\Pi$  OH molecular band system (0–0 band R and Q branches at 306–308 nm and 1–0 band R and Q branches at 281 nm) and the  $A^3\Pi - X^3\Sigma^-$  NH molecular band system (0–0 band R and Q branches at 330 and 336 nm) [29]. These molecular emissions are readily apparent at delay times approaching 40  $\mu$ s, long after any atomic emission (from hydrogen or atmospheric atomic nitrogen and oxygen) has disappeared. Using a suitably high-resolution Echelle spectrometer, individual rotational transitions are easily identifiable in the vibration bands, suggesting possible applications for molecular spectroscopy. While the plasma emission dependence on the ambient bath gas has been studied previously for LIBS on solids [30], and the molecular emission from such molecules as  $C_2$ , CN,  $N_2$ ,  $O_2$ , and air has been studied in a gas chamber [31] and on the surfaces of materials [32,33], the evolution of molecular emission from ablated liquids in various gases has not.

The use of molecular emissions from laser-induced plasmas in a variety of gas environments is starting to gain acceptance as a useful tool for sample diagnostics. In particular, Baudalet et al. have used native CN bond emission for the detection and identification of *E. coli* bacteria [34], Gluman has studied the formation of AlN molecules in plasmas from laser-ablated aluminum-containing nanopowders [35], Keszler has studied the formation of carbon molecules [33], and Portnov attempted to establish a correlation between the intensity ratios of the molecular emission from ablation byproducts and the molecular structure of the target by ablating aromatic hydrocarbons and nitroaromatic compounds [32]. These works indicate that the observation of molecular fluorescence can provide a useful technological tool for analysis, as well as a probe of environmental-dependent plasma chemistry.

In this work we investigate the difference in emission from atoms and molecules in a laser-induced plasma at the interface of ultra-pure water and three bath gases: air, argon, and nitrogen. Experimental parameters such as the laser pulse energy and the observation gate delay time were varied to optimize signal-to-noise ratios (SNR) and signal-to-background

ratios (SBR) in air. The absolute emission intensities were also studied. An atmospheric purge box was constructed to study these plasma emission characteristics in any desired bath gas. Lastly, plasma parameters such as the excitation temperature and the electron density were determined by measuring the ratio of the relative intensities and the Stark broadening of the  $H_{\beta}$  and  $H_{\gamma}$  emission lines observed in the plasma.

## 2. Experimental

The experimental apparatus used in all the experiments is shown schematically in Fig. 1. A Q-switched Nd:YAG laser (Spectra-Physics LAB-150) operating at its fundamental wavelength of 1064 nm generated laser pulses of 9 ns duration. This laser was capable of running at a repetition frequency of 10 Hz, but such a high repetition rate created violent disturbances on the surface of water, leading to excessive splashing on the optics and highly inconsistent breakdown events. In experiments on the surface of liquids, allowing as much time as possible between laser pulses is typically advantageous. In these experiments a single pulse every four seconds (set by the read-out time of the CCD camera) was used. Pulse energies were varied by attenuating the beam between 20 and 200 mJ/pulse by means of a half-waveplate and a Glan-laser polarizer.

The target water was contained in an eight cm diameter 200 mL Pyrex dish mounted on a vertical translation stage for precise alignment of the water surface in the laser focal region. A 39 mm focal length plano-convex lens was used to focus the laser. To avoid splashing on this lens, the beam was tilted with respect to the surface of the water, making an angle of incidence of 53° (see side view, Fig. 1(b)).

A one meter long 600  $\mu$ m quartz optical fiber located approximately 1 cm away from the ablation microplasma collected and transmitted the plasma emission to an Echelle spectrometer with fiber-coupled input slits (LLA, ESA3000). This spectrometer utilized a 1024  $\times$  1024 CCD-array (24  $\mu$ m  $\times$  24  $\mu$ m pixel area) with an image-intensifier (ICCD) and was controlled by a PC running manufacturer-provided software. The PC controlled not only the gating (shuttering) of the ICCD, but also controlled operation of the pulsed-laser via an on-board fast pulse generator to eliminate jitter in the time between laser pulse and plasma observation. The useful spectral range of the spectrometer was 200–834 nm with a 0.005 nm resolution in the UV. The end of the fiber near the water surface was mounted on a fully articulated x–y–z translation stage for precise control of its location.

In all cases, 50 individual laser pulses were averaged together to perform one measurement. At high pulse energies, it was found that the surface of the water would drop appreciably after several 50-pulse measurements due to splashing out of the sample dish and laser-induced evaporation. This drop in surface level was enough to change the resulting beam intensity at the water surface, causing a noticeable decrease in LIBS signal intensity. To avoid this systematic decrease in intensity and to increase day-to-day reproducibility of the water/gas interface location, the dish was filled until overflowing, and allowed to form a meniscus. All experiments were performed at the meniscus/gas interface which had a highly reproducible location. At the beginning of every set

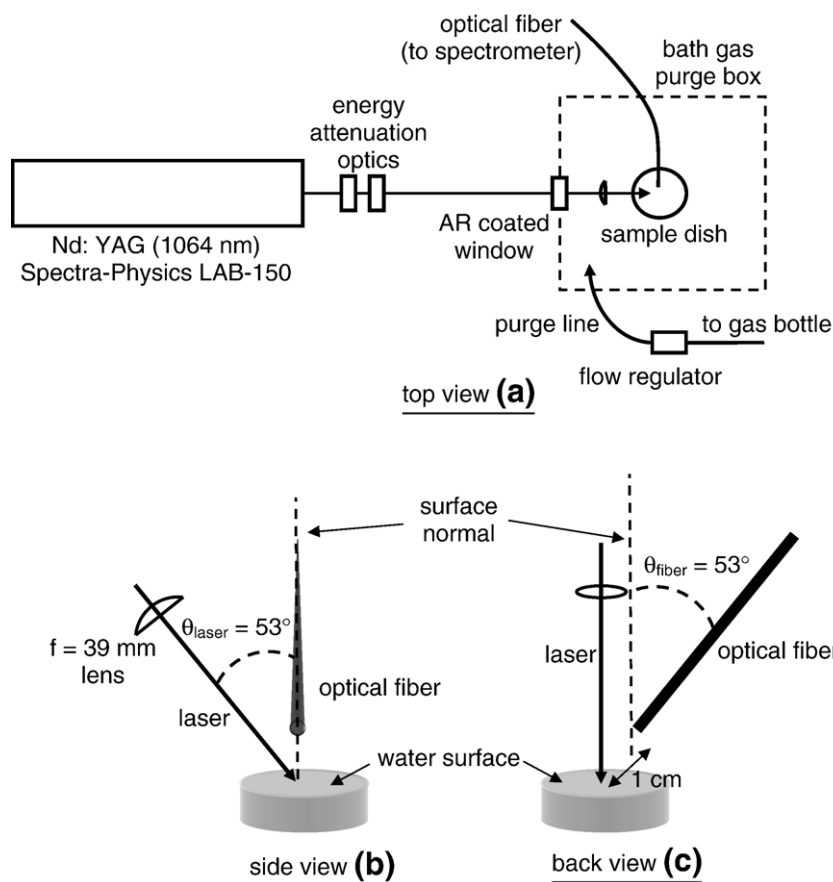


Fig. 1. The experimental setup used to perform LIBS on water. (a) An overhead view of the apparatus. The path of the laser is indicated by a solid line, while the purge box utilized to change the bath gas at the water/gas interface is indicated with a dashed line. (b) A side view of the surface of the water showing the geometry of the laser beam and the optical fiber used to collect the plasma emission. The normal to the surface of the water is shown and the laser has an AOI of  $53^\circ$ . (c) A back view of the surface of the water showing the orientation of the optical fiber which also has an AOI of  $53^\circ$ .

of measurements, the vertical position of the sample dish and the position of the fiber tip were adjusted to optimize the plasma emission from the hydrogen  $H_\beta$  line, minimize the contribution from atmospheric nitrogen and oxygen, and to make the spectrum identical to spectra obtained on previous days. In this way, highly reproducible spectra were obtained from measurements spanning many weeks. Between 50-pulse measurements, additional water was added to the sample dish by means of a funnel placed near the surface until the water overflowed the dish. The meniscus was allowed to settle to its reproducible location. As a result, we eliminated the long-term decrease in emission intensity and reduced the fractional uncertainty on the absolute (non-normalized) emission intensity of any atomic line to the 10% level.

A polyacrylic bath gas purge box approximately  $0.02 \text{ m}^3$  (roughly  $1 \text{ ft}^3$ ) was constructed around the entire sample dish/translation stage/focusing lens assembly. The laser entered the purge box through an anti-reflection coated window. A flow of gas ( $>1 \text{ scfh}$ ) was permitted into the box through a 6.35 mm diameter polyethylene hose. The purge box was not air tight, creating a near-atmospheric positive-pressure purge-gas environment above the surface of the water. Standard industrial grade argon and nitrogen bottles were used as the gas source.

All experiments utilized ultra-purified water ( $<1 \text{ ppm}$  any trace contaminants). The water was pre-filtered by a commercial

water filtration system which first purified the water by granulated activated carbon-filtration with UV lamps and reverse osmosis (Omnipure) and then ultra-purified the water to a resistance of  $18.2 \text{ M}\Omega$  (U.S. Filter, Purelab Plus UV/UF).

### 3. Results and discussion

LIBS spectra were acquired from the ablation of water in all three bath gases (air, argon, and nitrogen) as a function of laser pulse energy and as a function of delay time after the laser pulse. In all cases the exposure time of the image intensifier (typically referred to as the “gate width”) was  $20 \mu\text{s}$ . The laser had a maximum energy of  $650 \text{ mJ/pulse}$ , but our study was limited to the range of  $20 \text{ mJ}$  to  $200 \text{ mJ}$ . This was done to overlap with previously performed experiments [4,28] and due to practical constraints. Specifically, the probability of breakdown fell below 50% at pulse energies below  $20 \text{ mJ}$ , and at pulse energies above  $200 \text{ mJ}$  little to no increase in emission intensity was observed (due to plasma shielding) while the amount of optics-contaminating splashing greatly increased.

The time delay between the laser pulse and electronic activation of the image intensifier (which will be referred to hereafter as the “gate delay time” or “delay time”) was varied from  $1 \mu\text{s}$  to  $40 \mu\text{s}$ . As mentioned earlier, atomic emission in air



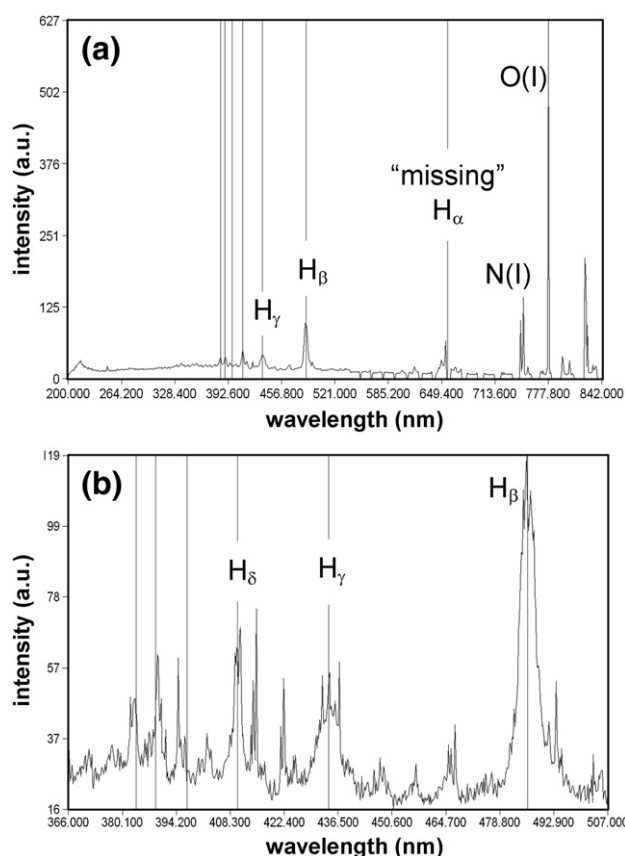


Fig. 2. A LIBS spectrum of  $\text{H}_2\text{O}$  ablated in an air environment observed at a delay time of 1  $\mu\text{s}$ . Vertical lines indicate the location of hydrogen emission lines. (a) Broadband spectrum showing the dominant atomic hydrogen emission lines ( $\text{H}_\beta$  and  $\text{H}_\gamma$ ) and the strongest oxygen and nitrogen emission lines from the atmospheric gas. The location where the  $\text{H}_\alpha$  line should be observed is denoted. (b) A close-up of the same spectrum from 366–507 nm. The three strongest observed hydrogen emission lines are identified. The hydrogen lines are significantly Stark-broadened compared to the much narrower nitrogen lines observable in this spectrum.

tended to cease by 6  $\mu\text{s}$ , with 10  $\mu\text{s}$  being the longest delay time at which any atomic emission could be observed. Conversely, molecular emission was still readily observable at delay times of 40  $\mu\text{s}$ . Typical LIBS spectra in these time regimes are shown in Figs. 2 and 3. Fig. 2(a) shows a LIBS spectrum of water obtained in air with a laser pulse energy of 100 mJ at a delay time of 1  $\mu\text{s}$ . Apparent in this spectrum are the four atomic emission lines studied in this work: the hydrogen-beta and hydrogen-gamma lines ( $\text{H}_\beta$  and  $\text{H}_\gamma$ ) at 486.134 and 434.047 nm respectively, a neutral nitrogen line (labeled N(I)) at 746.832 nm and the oxygen fine-structure triplet (labeled O(I)) at 777.194, 777.417, and 777.539 nm. In Fig. 2(a) the oxygen triplet appears unresolved, but at higher resolution the three emission lines are well resolved. Noticeably absent from the spectrum is the hydrogen-alpha ( $\text{H}_\alpha$ ) line at 656.27 nm which others have reported of dominating the spectrum of water [28]. This emission line fell in one of the spectral “gaps” in the Echelle spectrometer, which is a result of a mis-mapping of the Echelle diffraction pattern onto a CCD chip of finite size. The ESA3000 spectrometer utilized in this study was optimized for LIBS use specifically on metals where UV and near-UV emissions

dominate the spectrum. Thus gaps in spectral coverage did not start occurring until wavelengths  $>500$  nm. Although it is unfortunate that the  $\text{H}_\alpha$  line was not observed, previous studies have found that the first choice for the measurement of plasma parameters such as electron density should not be the stronger  $\text{H}_\alpha$  line, but rather the  $\text{H}_\beta$  line [5]. It was found that the  $\text{H}_\alpha$  line was suitable in cases where the electron density was lower than  $10^{17} \text{ cm}^{-3}$ , but at higher densities proved to be highly susceptible to self-absorption which distorted the emission profile.

Fig. 2(b) shows a close-up view of the spectral region 366–507 nm containing the three strongest hydrogen emission lines

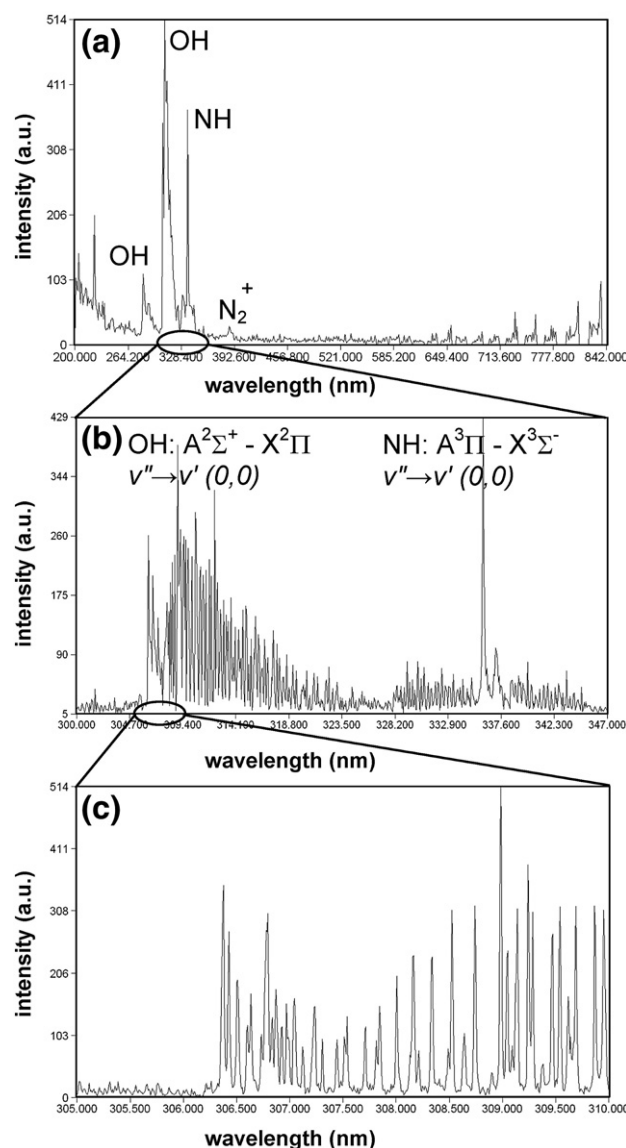


Fig. 3. A LIBS spectrum of  $\text{H}_2\text{O}$  ablated in an air environment observed at a 10  $\mu\text{s}$  time delay. The spectrum is composed entirely of molecular emission from the recombination of atoms liberated from the target and from the bath gas. (a) Broadband spectrum from 200–840 nm showing the dominant molecular emissions from OH, NH, and  $\text{N}_2^+$ . (b) A close-up of the same spectrum from 300–347 nm showing a vibrational band from an NH and an OH band system. Each band is composed of hundreds of rotational transitions. (c) A close-up of the spectrum from 305–310 nm. Each rotational transition in the OH band is clearly resolved with high signal-to-noise.

(after  $H_{\alpha}$ ): the  $H_{\beta}$ ,  $H_{\gamma}$ , and  $H_{\delta}$  lines. In this figure, the Stark broadening of the hydrogen lines is readily apparent, compared to the much narrow nitrogen lines interspersed throughout the spectrum. Although the  $H_{\delta}$  line and two other hydrogen emission lines are visible in this spectrum (vertical lines mark the location of the hydrogen transitions), in low signal-to-noise experiments these lines were not easily resolved and were often contaminated by atomic oxygen and nitrogen lines, making it impossible to accurately measure their intensity. Therefore our analysis of atomic hydrogen was limited to the  $H_{\beta}$  and  $H_{\gamma}$  lines.

Fig. 3 shows a typical LIBS spectrum of water obtained in air with a pulse energy of 100 mJ and a delay time of 10  $\mu$ s. Fig. 3 (a) shows the entire spectral range from 200 to 840 nm. This spectrum is dominated by two molecular band systems: the OH  $A^2\Sigma^+ - X^2\Pi$  band system and the NH  $A^3\Pi - X^3\Sigma^-$  band system. Although many bands from these two band systems are visible, the most easily discerned are the OH 0–0 band (R and Q branches from 306–308 nm), the OH 1–0 band (R and Q branches at 281 nm), and the NH 0–0 band (R and Q branches at 330 and 336 nm). Other molecular band systems are in evidence in this spectrum including systems from NO and  $N^+_2$ . In particular, the UV end of the spectrum below 250 nm seems to be dominated by unresolved components of the NO  $A^2\Sigma^+ - X^2\Sigma^+$  ( $\gamma$  band) system. Fig. 3(b) shows a zoomed in view of the spectral region 300–348 nm, containing two vibrational bands. The OH 0–0 band (degrading red) is visible near 309 nm with a very sharp R branch band head at 306 nm. The NH 0–0 band is centered at 336 nm. This headless band contains a very narrow line-like feature at 336.01 nm which is the 0–0 Q branch which is flanked by the much less intense line-like Q branch of the 1–1 band. The much smaller peaks are also bands of this band system. Fig. 3(c) shows the excellent signal-to-noise of the OH 0–0 band. Each band is composed of hundreds of well defined rotational transitions, each completely resolved by the Echelle spectrometer.

Along with the four neutral atomic emission lines shown in Fig. 2(a), the OH and NH vibrational bands shown in Fig. 3(b) were studied in this work as a function of incident laser pulse energy and gate delay time. Regions of empty spectrum near the emission line or band were averaged to establish a background. The standard deviation of this empty background region was calculated and this value was defined to be the noise of that emission feature. Since there were many very small and unresolved yet reproducible molecular bands in different parts of the spectrum, and since the background Bremsstrahlung and continuum emission contributed more heavily to the noise and background in the ultraviolet region of the spectrum, it was more consistent to define this type of “local” noise as opposed to a single “global” value of noise for the entire spectrum.

The area under the background-subtracted curve for the four atomic and two molecular emissions was then numerically integrated to obtain an absolute emission intensity. This was done primarily because it was impossible to find the areas via non-linear least-squares curve fitting of the hundreds of small rotational transitions in the molecular bands. These emission intensity values were then used to calculate the SNR and the SBR. For our later studies of Stark-broadening of the hydrogen

lines, nonlinear least-squares fitting with a Lorentzian lineshape was performed on relevant parts of the spectrum to obtain an accurate measurement of peak width.

Uncertainties on all our measurements were obtained by comparing the scatter of repeated measurements and calculating the standard deviations of observed quantities. Reported uncertainties, unless otherwise noted, are one-sigma standard deviations.

### 3.1. Laser-pulse energy dependence in air

Fig. 4 shows the results of the analysis of the SBR, SNR, and emission intensities as the laser pulse energy was varied from 20 mJ to 200 mJ with the image intensifier gate delay set to 2  $\mu$ s for all experiments. Values were measured for the four atomic emission lines: the  $H_{\beta}$  and  $H_{\gamma}$  lines at 486.134 and 434.047 nm, the N(I) line at 746.832 nm and the O(I) fine-structure triplet at 777.4 nm, as well as for the two molecular vibrational bands: the OH 0–0 band at 307 nm and the NH 0–0 band at 336 nm. In all four graphs, the functional dependence of the two molecular transitions is almost identical, yet show consistent differences compared to the behavior of the four atomic emissions. The atomic emission lines show near identical dependence on laser pulse energy regardless of whether the atom was ablated from the sample (H), was contributed from the bath gas (N), or was a combination of the two (O).

Fig. 4(a) shows the unnormalized SBR for the four atomic species. The data were fit by a weighted, scaled-linear function after plotting the data on a log-linear scale to most clearly highlight the difference between the behavior of the molecular emission and the atomic emission. Although a decaying exponential function could have been used to fit this data, it was not the intent to imply an exponential dependence of the SBR with pulse energy and the scaled linear function yielded the lowest reduced  $\chi^2$ . The slopes of these weighted fits were very similar and are shown in Fig. 4(a). For the 2  $\mu$ s gate delay, these atomic species showed a slight SBR maximum around 40 to 60 mJ, then a near linear decrease with increasing laser pulse energy. Fig. 4(b) shows the unnormalized SBR for the two molecular species on the same scale as Fig. 4(a). These SBR values also reached a slight maximum around 20–40 mJ, but then decreased almost 8 times more quickly as the pulse energy was increased. The slopes of these fits were also very similar, yet were an order of magnitude larger than the slopes of the atomic species fits.

Fig. 4(c) shows the normalized SNR for the 6 transitions. Each data set was normalized to its value at 200 mJ to show its dependence on laser pulse energy. These data were fit by a weighted linear function and are plotted on a log-lin scale. The slopes of these fits are reported on the graph. Again the behavior of the two molecular emissions was almost identical, yet distinct from the behavior of the four atomic transitions. Most surprisingly, the two molecular emissions possessed a negative slope after reaching a slight maximum at 40–60 mJ, indicating a slight decrease in SNR as a function of pulse energy, while the atomic emission demonstrated a marked increase in SNR with increasing pulse energy.

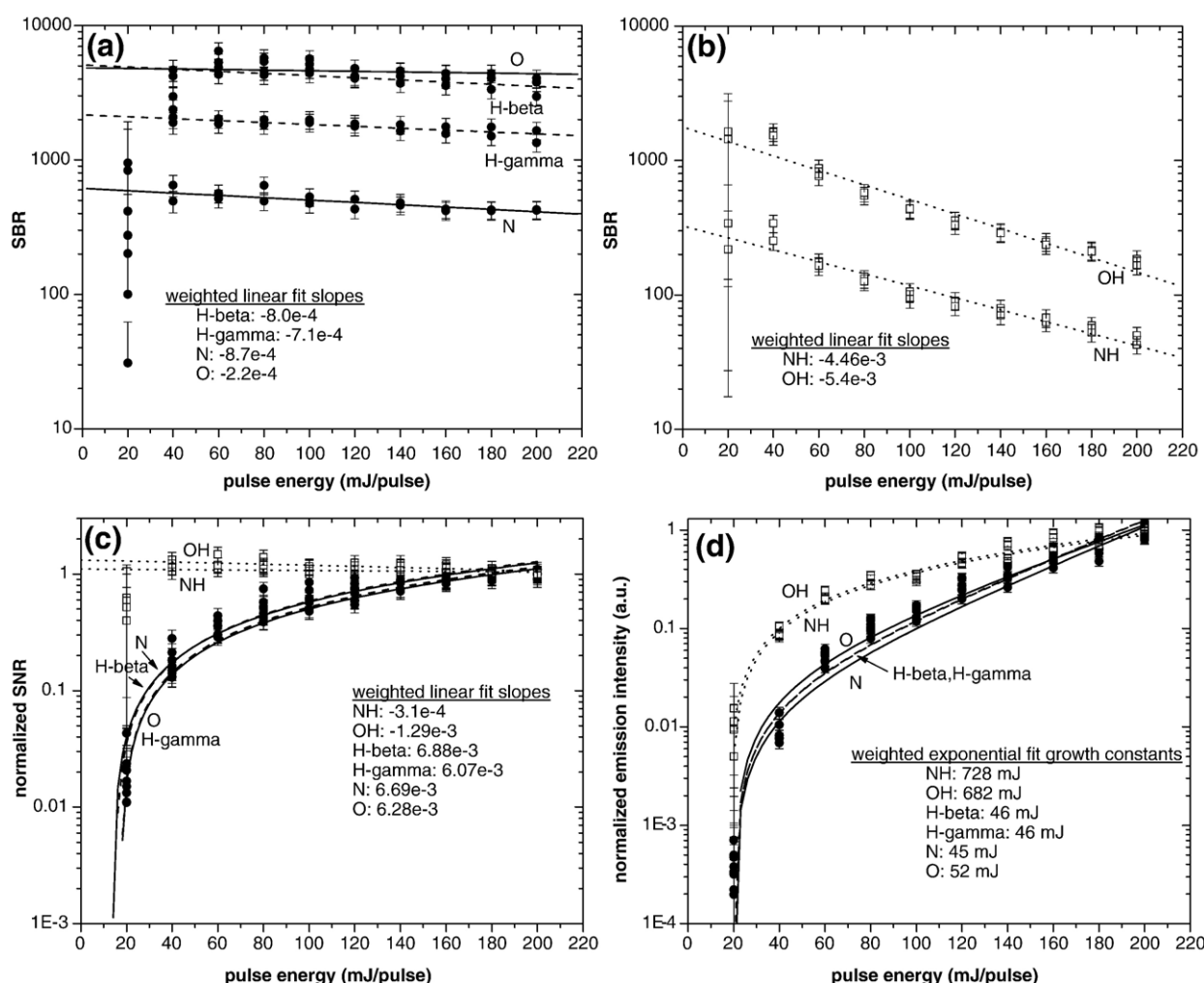


Fig. 4. Molecular and atomic LIBS emission as a function of ablation laser pulse energy. (a) SBR dependence for the four atomic (●) transitions described in this work. Dashed lines are linear fits to atomic hydrogen emissions, and solid lines are linear fits to N and O emissions. (b) SBR dependence for the two molecular (□) transitions described in this work. (c) SNR dependence for the six transitions. Data for each transition are normalized to their value at 200 mJ and have been fit with a linear function. (d) Absolute emission intensity dependence for the six transitions. Data for each transition are normalized to their value at 200 mJ and have been fit by an exponential growth function.

Fig. 4(d) shows the normalized emission intensity for the 6 transitions. These data were obtained by normalizing the integrated areas under the emission profile by the value at 200 mJ. Again, the differences between the molecular emissions and the atomic emissions were quite noticeable. These data were fit by a weighted exponential growth function of the form  $\exp(E/E_0)$ , where  $E$  is the pulse energy and  $E_0$  is the exponential growth constant reported in the graph. The molecular emission had an exponential growth constant almost 15 times greater than the atomic emission, demonstrating a much weaker dependence on pulse energy than the atoms possessed.

It is significant that when using this particular gate delay time and width to observe molecular fluorescence, the absolute emission intensity increased with increasing laser pulse energy as expected, but the SBR and SNR decreased with increasing energy. This suggests that any attempt to detect the presence of a particular species in a liquid target by observing resultant molecules with these temporal detector conditions should be done at the lowest possible pulse energy that still yields

significant emission. This is also the most convenient regime to work in experimentally, as was noted above.

### 3.2. Gate delay time dependence in air

The time delay between the ablation laser pulse and the observation of the plasma emission is of primary importance in most LIBS experiments. Appropriate gate delay times are chosen based on the requirements of the experiment (i.e. maximum signal-to-noise, maximum emission intensity, smallest background, etc.). Fig. 5 shows the results of varying the gate delay time from 1  $\mu$ s to 40  $\mu$ s. All the results in Fig. 5 were obtained using a pulse energy of 100 mJ/pulse. Two non-consecutive measurements were performed at each delay time, both of which are shown in Fig. 5. In Fig. 5(a) and (b) the SBR for the H $\beta$ , NH, and OH emission are shown as a function of the gate delay time. Fig. 5(a) shows the atomic H $\beta$  SBR and Fig. 5(b) shows the molecular NH and OH SBR on the same scale. The data are normalized to the maximum value of the average of

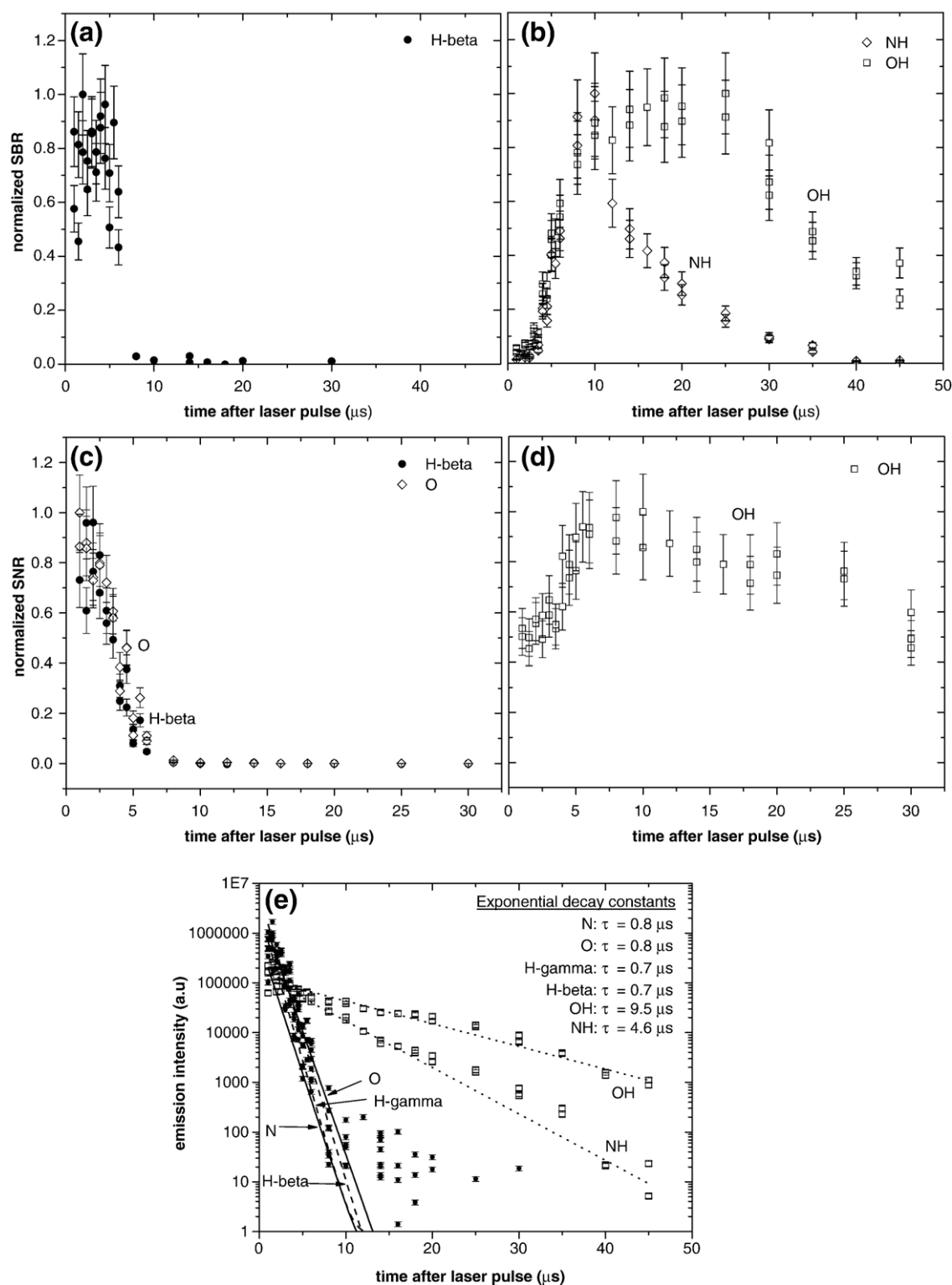


Fig. 5. The dependence of LIBS emission on gate delay time. (a) SBR dependence for the  $\text{H}_{\beta}$  atomic emission (closed symbol) and (b) the NH and OH molecular emissions (open symbols). Data have been normalized to their maximum value. (c) SNR dependence for the  $\text{H}_{\beta}$  and O atomic emissions and (d) the OH molecular emission. Data have been normalized to their maximum value. (e) Absolute emission intensity dependence for the two molecular ( $\square$ ) and four atomic ( $\bullet$ ) emissions described in this work. Data for each transition have been fit by an exponential decay function and the decay constant is given. Dotted lines are fits to molecular emissions, dashed lines are fits to atomic hydrogen emissions, and solid lines are fits to N and O emissions.

the two measurements. The hydrogen emission SBR was either rising slowly or was relatively constant from 1 to 5  $\mu\text{s}$  (within the noise of the measurement), then dropped sharply to almost

zero by 10  $\mu\text{s}$ . Conversely, the SBR of the NH and the OH molecular emissions increased simultaneously from zero to achieve their maximum value of SBR around 10  $\mu\text{s}$ . The NH



SBR then dropped slowly, while the OH emission stayed relatively constant until approximately 25  $\mu\text{s}$ . At 40  $\mu\text{s}$  after the laser pulse, the OH molecular emission still exhibited a significant SBR.

Fig. 5(c) and (d) show the SNR as a function of delay time for the OH molecular emission and the  $\text{H}_\beta$  and O atomic emission. Fig. 5(c) shows the atomic  $\text{H}_\beta$  and O SNR and Fig. 5(d) shows the molecular OH SNR on the same scale. These data are normalized to the maximum value of the average of the two measurements. The two atomic species demonstrated a consistent near-linear decrease in signal-to-noise from 1 to 6  $\mu\text{s}$ . The SNR was zero (within the uncertainty) beyond approximately 8  $\mu\text{s}$ . The OH SNR increased to its maximum value within the same time frame as the atomic species SNR decreased. The OH SNR then remained fairly constant for an extremely long range of delay times, roughly out to 25  $\mu\text{s}$ , at which time it began to decrease toward zero. The NH SNR dependence is not shown, but behaved similarly to OH.

Fig. 5(e) shows the absolute integrated emission intensity for the six transitions. A decaying exponential function of the form  $\exp(-t/\tau)$  has been fit to the data. The emissions from all four atomic species exhibited identical dependence on gate delay time, decreasing exponentially until approximately 10  $\mu\text{s}$ , at which time the signal was effectively zero. The intensity of the emissions from the two molecular species also decreased exponentially, but at a much slower rate. The decay constants,  $\tau$ , obtained from the numerical fits are shown in Fig. 5(e) and show a rate of decrease in molecular emission intensity significantly slower than exhibited by the atomic species.

It is clear from Figs. 4 and 5 that inferring the presence of atomic species in samples from the emission of molecules formed after ablation requires substantially different experimental parameters than is required for optimal atomic emission observation. In particular, the observation of emission from hydrogen-containing molecules benefits from a reduction in laser pulse energy, as is shown in Fig. 4. Although the absolute emission increases with increasing pulse energy, the increase in optics contamination and irreproducibility from splashing and surface perturbation, along with the relative independence of observed SNR with pulse energy, all suggest that lower laser pulse energies are beneficial. In a similar fashion, the absolute emission intensity from molecules decreases with increasing observation delay time, but at a significantly slower rate than that of the atomic species. It is often desirable to delay the measurement gate until significant noise or “contaminating” atomic peaks have disappeared from the spectrum. Both NH and OH show a maximum SNR around 10  $\mu\text{s}$ , at which time atomic emission has ceased and background emission levels (which can be a significant source of noise at small delay times) are far reduced from values in typical LIBS experiments.

### 3.3. OH and $\text{H}_\beta$ dependence on bath gas

In the above experiments, NH was produced by the recombination of atomic hydrogen liberated by the laser-induced ablation of the water target and atomic nitrogen liberated from atmospheric  $\text{N}_2$  molecules in the microplasma.

OH exhibited slightly different behavior from NH due to the additional contribution of atomic oxygen in the microplasma from laser ablated water as well as from atmospheric  $\text{O}_2$  molecules. To study the behavior in non-atmospheric bath gases, the purge box surrounding the water target was filled with argon or nitrogen until a condition of near-atmospheric over-pressure of the new bath gas was created. The experiments described in Sections 3.1 and 3.2 were repeated in both these environments. Typical spectra obtained in each of the three bath gases at 100 mJ/pulse at a gate delay time of 10  $\mu\text{s}$  are shown in Fig. 6. Fig. 6(a) shows the spectra with no normalization. Notice that while the  $\text{H}_\beta$  emission was non-existent at delay times of 10  $\mu\text{s}$  in air and nitrogen, it was still quite strong, possessing excellent signal-to-noise, when the spectrum was obtained in argon. However in argon the OH emission was reduced and the NH emission was non-existent, as anticipated. In Fig. 6(a) the three spectra have been normalized to make their maximum values identical to highlight and accentuate their differences. In the argon bath gas, the dominant spectral feature was the O triplet at 777 nm — all of which was liberated from the ablated water. This is not surprising when one observes the substantial increase in  $\text{H}_\beta$  emission at 486 nm in the argon environment and the subsequent decrease in the formation of

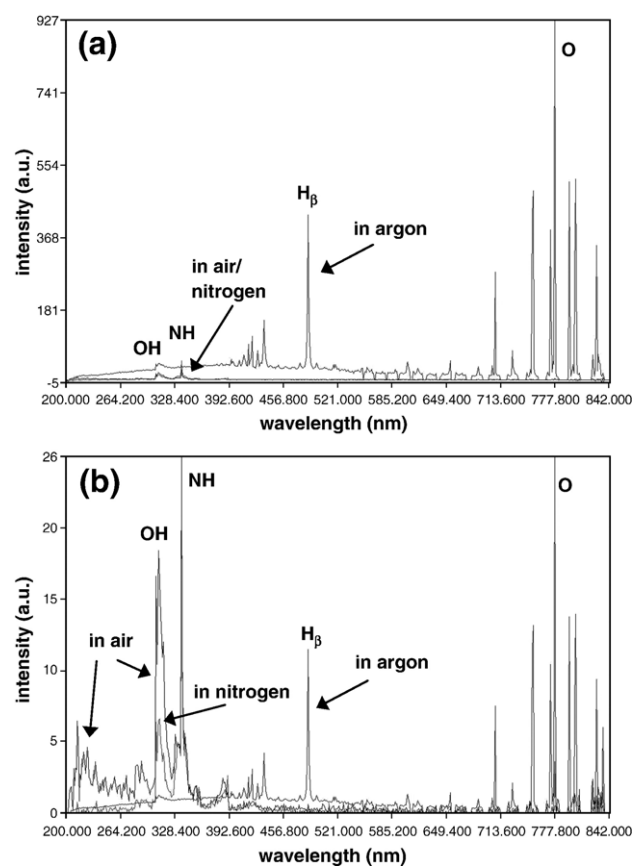


Fig. 6. LIBS emission spectra from a water surface in three bath gases: air, argon, and nitrogen. All data taken with 100 mJ/pulse laser energy at a gate delay time of 10  $\mu\text{s}$ . (a) Ablation in argon leads to an extreme enhancement in  $\text{H}_\beta$  emission with a corresponding decrease in OH emission and a complete absence of NH emission. (b) All three spectra have been scaled to make their maximum values identical.

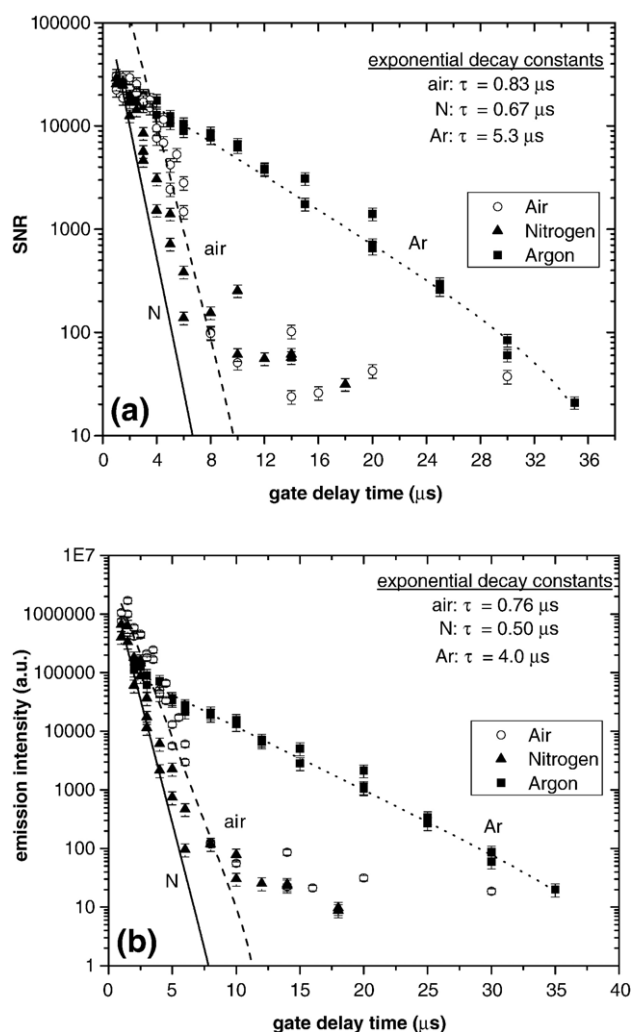


Fig. 7. H<sub>β</sub> emission in LIBS plasmas on a water surface in three different bath gases (■=argon, ○=air, ▲=nitrogen) as a function of gate delay time. The experimental results were fit to a decaying exponential function and the resulting decay constants,  $\tau$ , are shown. Dotted lines are fits to argon data, dashed lines are fits to air data, and solid lines are fits to nitrogen data. (a) SNR in the three gases vs. delay time. (b) Absolute emission intensity of the H<sub>β</sub> emission in the three gases vs. delay time.

OH. In fact the integrated OH emission intensity at 10 μs is approximately an order of magnitude less intense in argon (and nitrogen) than it is in air. This is explored in more detail below.

In both the air and nitrogen the dominant spectral feature was the line-like Q-branch of the 0–0 band in NH at 336 nm. In Fig. 6(b), both the air and nitrogen spectra have been normalized to make this peak the same size. This feature was significantly more intense in the nitrogen than it was in air, but was not visible in the argon environment, as expected. The spectra taken in air and nitrogen were highly similar with the most significant difference being the decline in the amount of emission from molecular OH in the nitrogen environment as a result of a reduction of the number of free O atoms in the plasma. Due to the similarities in plasma parameters such as temperature and electron density (discussed below in Sections 3.4 and 3.5) a careful investigation of the reduction in the OH

emission seen in nitrogen as compared to air should allow one to estimate the fraction of O contributed from the atmosphere and the fraction from ablated molecular water in the atmospheric spectra. This was not attempted in this study.

The temporal evolution of the plasma H<sub>β</sub> emission in the three bath gases is shown in Fig. 7, which shows the SNR (Fig. 7(a)) and the absolute emission intensity (Fig. 7(b)) as a function of gate delay time. The measurements were again performed twice at each delay time and the results were fit by a weighted decaying exponential function of the form  $\exp(-t/\tau)$ . The decay constants from the fit,  $\tau$ , are given in the figure. The temporal evolution of the plasma was quite similar for ablation in the air and nitrogen bath environment, but the decay constant was almost an order of magnitude larger for ablation in the argon environment. At 10 μs (as shown in Fig. 6), the absolute H<sub>β</sub> emission intensity was almost a factor of 1000 more intense in the argon environment than in nitrogen or in air.

Also of interest is the behavior of the OH molecular emission in the three bath gases. As seen in air, the SBR of the OH emission in Ar and N rose as a function of gate delay time to a maximum in the region of 15 to 20 μs. Also as seen previously in air, the SBR decreased exponentially with increasing laser pulse energy in all gases. The argon SBR decreased most quickly, with an exponential decay constant only one-half of what was measured in air or nitrogen.

The SNR of the OH molecular emission was relatively constant as a function of incident laser pulse energy in all gases (see the behavior in air in Fig. 4(b)). However, the dependence on delay time was markedly different in air than it was in argon or nitrogen. Fig. 8(a) shows the SNR of the OH emission in air and argon, both measurements performed with an incident laser pulse energy of 100 mJ. For clarity, nitrogen has been omitted from this figure. In both plasmas, the OH emission SNR was approximately the same at very early delay times. However, in air it showed an immediate increase with increasing delay time and possessed a relatively flat dependence from 5 to 20 μs. In argon the SNR dropped immediately, with no increase as a function of delay time and demonstrated a fairly uniform exponential decrease with increasing delay times.

As expected, the absolute emission intensity shown in Fig. 8(b) decreased with increasing delay times. However, at no time was the value of the absolute emission intensity from OH in argon greater than it was in air (unlike the atomic H<sub>β</sub> emission). This can be seen qualitatively in Fig. 6(a) where the OH emission is noticeably smaller in argon than in air. Not only was the absolute emission intensity different in the two gases, but the time-dependent rate of decrease was different as well. In air the emission intensity exhibited strong non-exponential behavior, with roughly three different regimes identifiable: from 0 to 5 μs, from 5 to 25 μs, and at delay times greater than 25 μs. In argon the emission intensity exhibited a much smoother exponential-like decrease with delay time.

### 3.4. Excitation temperature dependence on bath gas

Plasma temperatures were measured in each of the three bath gasses as a function of laser pulse energy and gate delay time.

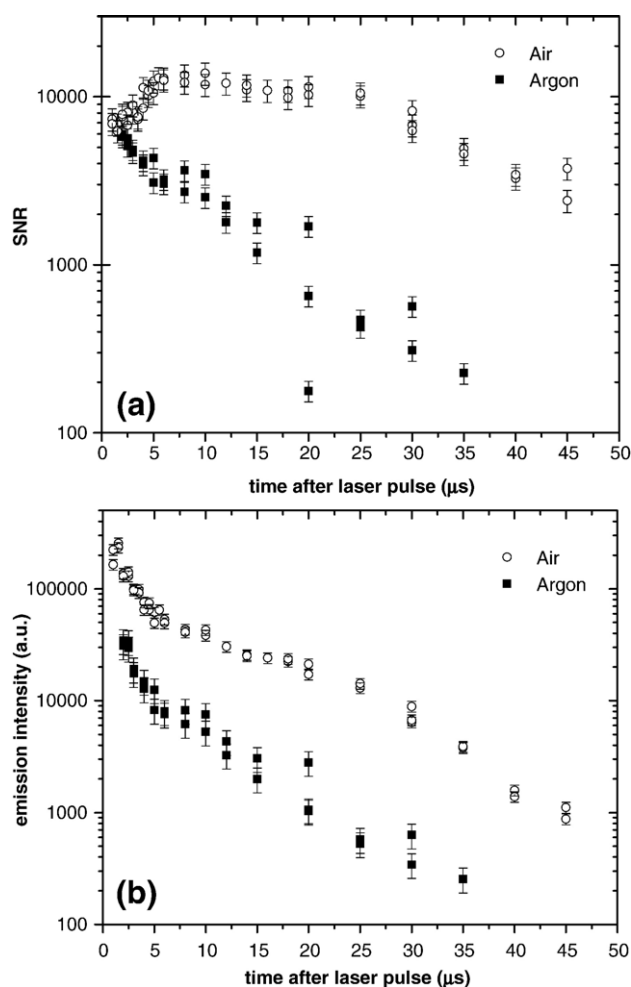


Fig. 8. Molecular OH emission in a LIBS plasma on a water surface in two different bath gases (■=argon, ○=air) as a function of gate delay time. (a) SNR of the OH emission. (b) Total integrated intensity of the OH emission.

Results are shown in Fig. 9. The plasma temperatures were determined from the ratio of the  $H_{\beta}$  and  $H_{\gamma}$  emission intensities using the equation commonly used for obtaining plasma excitation temperatures from the emission intensities of two neutral lines:

$$\frac{I_1}{I_2} = \frac{g_1 A_1 \lambda_2}{g_2 A_2 \lambda_1} \exp\left(-\frac{|E_1 - E_2|}{kT_e}\right) \quad (1)$$

The indices 1 and 2 identify each individual line,  $gA$  is the product of the statistical weight and the Einstein coefficient for spontaneous emission,  $\lambda$  is the emission wavelength,  $k$  is the Boltzmann constant,  $T_e$  is the excitation temperature and  $E_1 - E_2$  is the energy difference of the upper state energies of the two lines used in the calculation. In this case  $E_{H_{\beta}}^{\text{upper}} = 12.75$  eV,  $E_{H_{\gamma}}^{\text{upper}} = 13.06$  eV, so  $|E_1 - E_2| = 0.31$  eV. Uncertainties for the temperatures were calculated using the procedure suggested by Simeonsson and Miziolek [36], with a fractional uncertainty in the ratio of the emission lines of 0.14. Typical uncertainties are 30–50% for these measurements. In Fig. 9(a), all data was obtained at a delay time of 2  $\mu\text{s}$  and in Fig. 9(b) the laser pulse energy was kept constant at 100 mJ/pulse. In neither case did the

plasma temperature show a great dependence on the bath gas, although the plasmas formed in nitrogen tended to be the least hot of all three. Fig. 9(a) shows that the plasma temperature in all three gases was relatively insensitive to increases in laser pulse energy, most likely due to self-shielding of the plasma. Lastly, the plasma temperatures tended to decrease with increasing gate delay time leading to the strong decrease in emission intensity observed earlier. In fact, the temperatures of plasmas formed in air could not be obtained at 10  $\mu\text{s}$  due to the inability to measure the intensity of the  $H_{\gamma}$  emission line. It should be noted that an increase in temperature at 10  $\mu\text{s}$  in plasmas formed in argon is not implied by Fig. 9(b), rather the noise on the measurement makes this result consistent with a linear decrease in temperature. It is probable, however, that at 10  $\mu\text{s}$ , plasma temperatures in argon are still around 10,000 K, explaining the strength of the  $H_{\beta}$  emission line which is clearly visible at this delay time in Fig. 6.

For all three bath gases, tests were performed to verify the plasma's "optical thinness" for all pulse energies and delay times [36–38]. Due to the use of ultra-pure water, no suitable analyte lines were visible in the spectrum for the observation of

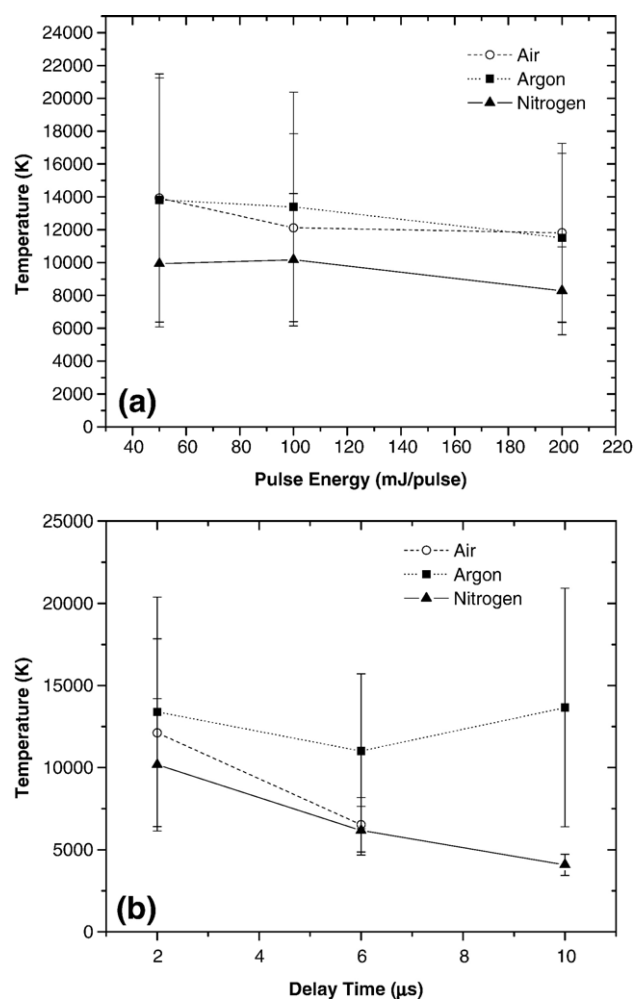


Fig. 9. Plasma excitation temperatures calculated from the ratio of  $H_{\beta}$  and  $H_{\gamma}$  emission intensities as a function of (a) laser pulse energy and (b) delay time in three different bath gases (■=argon, ○=air, ▲=nitrogen). Lines are provided as a guide to the eye only. Dotted lines connect argon data, dashed lines connect air data, and solid lines connect nitrogen data.

self-reversal or self-absorption. Therefore, as suggested by Samek et al. [5], the three components of the oxygen triplet at 777 nm were analyzed to confirm that their measured intensity ratios were consistent with those predicted by the statistical weights of the upper levels [36]. In all cases, the measurements within their uncertainty were consistent with the expected ratio of 7:5:3.

### 3.5. Electron density dependence on bath gas

The widths of the Stark-broadened  $H_\beta$  and  $H_\gamma$  emission lines were used to calculate the plasma electron density,  $N_e$ . Hydrogen and hydrogen-like ions exhibit an enhanced line broadening due to the linear Stark effect and measurements of the linewidth can be used to calculate the electron density using the relation [39]

$$N_e = C(N_e, T) \Delta\lambda_{FWHM}^{3/2} \quad (2)$$

In this expression  $\Delta\lambda_{FWHM}$  is the actual full-width-at-half-maximum of the transition and the parameter  $C$  is a function that depends only weakly on the electron density,  $N_e$  and  $T$ . Although Eq. (2) technically defines a transcendental function,  $C$  can normally be considered a constant within the range of experimental parameters used in this work, assuming the plasma temperature is known. The constant,  $C$ , used to calculate  $N_e$  is tabulated in reference [39].

To determine the actual transition linewidth  $\Delta\lambda_{transition}$ , the measured linewidth,  $\Delta\lambda_{measured}$ , must be deconvolved from the instrument response function,  $\Delta\lambda_{instrument}$ . As pointed out by Samek et al. [5] the convolution of narrow spectrometer slit functions gives rise to a line intensity distribution that can be approximated very well by a Lorentzian profile, making the deconvolution of the actual linewidth straightforward:

$$\Delta\lambda_{measured} = \Delta\lambda_{transition} + \Delta\lambda_{instrument}$$

Lorentzian functions were fit to both the  $H_\beta$  and  $H_\gamma$  emission profiles in the data using a non-linear least squares fitting routine and the FWHM was determined from these fits. To determine the spectrometer line broadening  $\Delta\lambda_{instrument}$ , Lorentzians were fit to isolated atomic lines in spectra obtained from low pressure Zn and Hg emission lamps which were used to calibrate the instrument. These measurements revealed a maximum instrument linewidth of  $0.020 \text{ nm} \pm 0.009 \text{ nm}$ . No Stark-broadened LIBS linewidths less than 0.1 nm were measured in this study, with the vast majority of all measurements greater than 1.0 nm. Thus the instrument linewidth and its related uncertainty only contribute a small fraction to the uncertainty of the true Stark-broadened linewidth,  $\Delta\lambda_{transition}$ . The linewidths for both the  $H_\beta$  and  $H_\gamma$  transitions are shown in Fig. 10 for ablation in all three bath gases as a function of the gate delay time (Fig. 10(a)) and laser pulse energy (Fig. 10(b)). The delay time measurements were all performed with a pulse energy of 100 mJ/pulse but the pulse energy measurements were not all performed at the same delay time. The delay time was chosen to correspond to a maximum in the SBR to reduce the presence of contaminating emission peaks. For air and

nitrogen this corresponded to 2  $\mu\text{s}$ , but for argon it was 6  $\mu\text{s}$ . Inspection of Fig. 10(a) shows that the Stark-broadening of both hydrogen transitions was reduced in argon, but did not decrease nearly as quickly as in air or nitrogen, exhibiting significant broadening out to at least 30  $\mu\text{s}$ . Also, the dependence on pulse energy shown in Fig. 10(b) was much less sensitive in argon than it was in the other two gases, increasing only slightly with increasing pulse energy. In all cases, the Stark broadening of the  $H_\gamma$  line was greater than the broadening of the  $H_\beta$  line, which is consistent with previously reported observations [5].

It should be noted that for water ablation, a strong contaminating oxygen line at 436.826 nm is present on top of the  $H_\gamma$  profile (stronger in air environments than in argon or nitrogen). Due to the strength of the linear Stark effect, the  $H_\gamma$  line was significantly (an order of magnitude) broader than the oxygen emission line. It was therefore possible to “eliminate” the oxygen line from the  $H_\gamma$  profile and compare the FWHM obtained both with and without the presence of the oxygen line. We estimate that the presence of this line in a spectrum with a

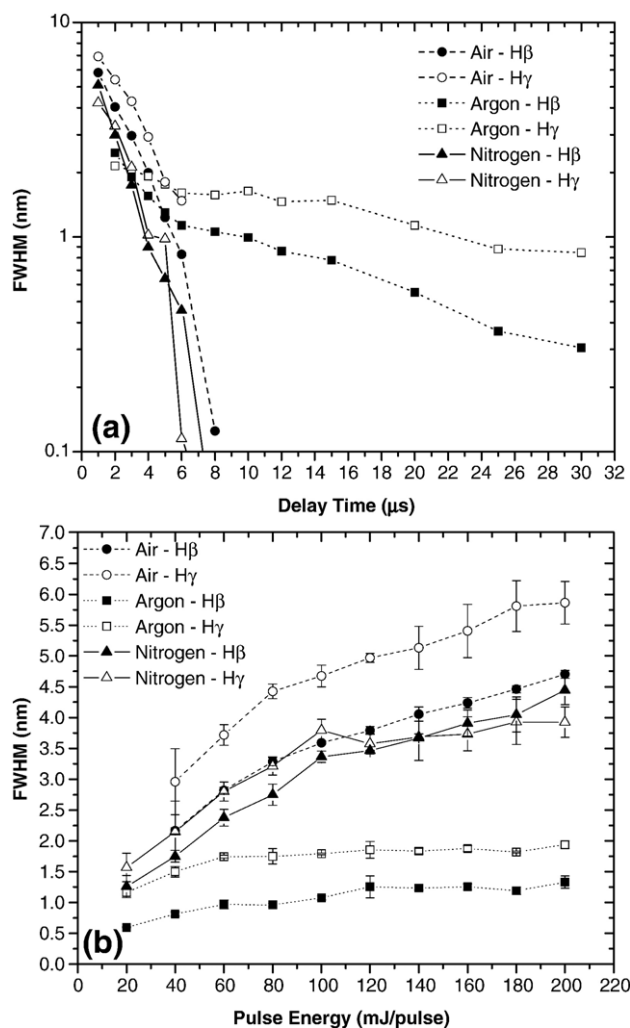


Fig. 10. Stark-broadened  $H_\beta$  (closed-symbol) and  $H_\gamma$  (open-symbol) linewidths for laser-ablated water in three bath gases (■=argon, ○=air, ▲=nitrogen). (a) Dependence on gate delay time – pulse energy constant at 100 mJ/pulse. (b) Dependence on laser pulse energy – delay time constant at 2  $\mu\text{s}$  for air and nitrogen, 6  $\mu\text{s}$  for argon.



suitably strong  $H_\gamma$  line contributed no more than 5% to our calculation of the  $H_\gamma$  FWHM.

These instrument-corrected Stark-broadened linewidths for both the  $H_\beta$  and the  $H_\gamma$  transition were used to calculate the electron density,  $N_e$ , using Eq. (2). The calculated electron densities as a function of laser pulse energy and gate delay time in the three bath gases are shown in Fig. 11. The calculated electron densities and the calculated “critical electron density” are shown for each gas. Calculation of this critical density,  $N_{e,crit}$ , is a standard method for determining whether the assumption of local

Table 1

Comparison of laser-induced plasma properties

	This work	Samek et al. <sup>a</sup>	Charfi et al. <sup>b</sup>
Pulse energy (mJ)	180–200	20–60	180
Laser $\lambda$ (nm)	1064	1064	1064
Pulse duration	9 ns	4–8 ns	7 ns
Line used to calculate $N_e$	$H_\beta$	$H_\beta$	$H_\alpha$
Delay time ( $\mu$ s)	1	1	1
$T(K)$	9395	7020	17,500
$N_e (\times 10^{16} \text{ cm}^{-3})$	15	14	300
Delay time ( $\mu$ s)	2	2	2
$T(K)$	11,822	6650	11,000
$N_e (\times 10^{16} \text{ cm}^{-3})$	10	8.5	150
Delay time ( $\mu$ s)	6	6	5
$T(K)$	6531	5685	5500
$N_e (\times 10^{16} \text{ cm}^{-3})$	0.83	1.7	10

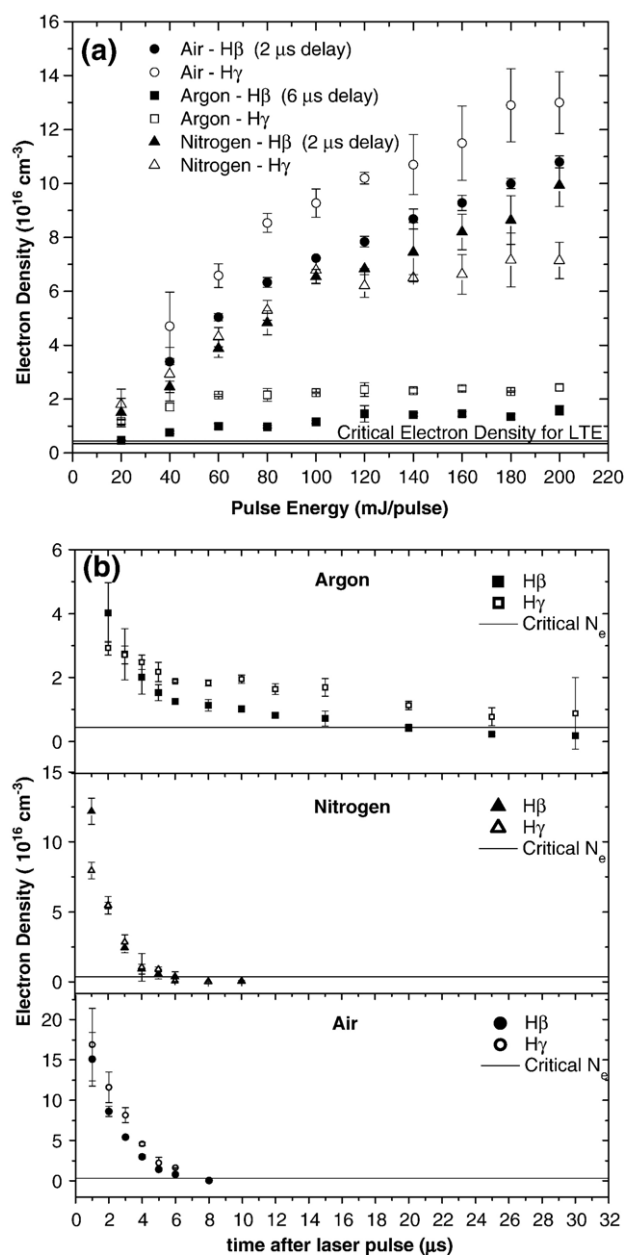
<sup>a</sup> Ref. [5]<sup>b</sup> Ref. [28]

Fig. 11. Electron densities calculated from Stark-broadened linewidths of  $H_\beta$  (closed-symbol) and  $H_\gamma$  (open-symbol) for laser-ablated water in three bath gases ( $\blacksquare$ =argon,  $\circ$ =air,  $\blacktriangle$ =nitrogen). (a) Dependence on laser pulse energy–delay time constant at 2  $\mu$ s for air and nitrogen, 6  $\mu$ s for argon. (b) Dependence on gate delay time–pulse energy constant at 100 mJ/pulse. In all graphs the critical electron density is shown on the graph as a horizontal line near 0.

thermodynamic equilibrium (LTE) is valid or not. We utilized a relationship suggested by Thorne [40] to define this quantity

$$N_{e,crit} = 1.6 \times 10^{12} \Delta E^3 T_e^{1/2} \quad (3)$$

where  $\Delta E$  (in eV) is the transition energy and  $T_e$  is the excitation temperature shown in Fig. 10. The condition of LTE is satisfied for all electron densities greater than  $N_{e,crit}$ . It is apparent from our measurements that the assumption of LTE was valid for all the regions where we could make accurate measurements of the emission intensities. For example,  $N_e$  falls below  $N_{e,crit}$  in air and nitrogen at delay times around 6 to 8  $\mu$ s. However, it was typically not possible to make a meaningful measurement of even the stronger  $H_\beta$  transition at these delay times.

A comparison of the temperature and electron density measurements obtained in air with previously reported results is presented in Table 1. The relevant experimental parameters, which were not identical in the three experiments, are provided and the temperatures and electron densities for three delay times are shown. Note that the use of the  $H_\alpha$  line by Charfi et al. leads to an overestimation of the electron density by at least an order of magnitude compared to the other results, as commented on earlier. This is apparent even at relatively low densities such as  $10^{16} \text{ cm}^{-3}$ .

#### 4. Conclusion

LIBS has been performed at the interface of a bulk pure water sample and three bath gases: air, nitrogen, and argon. The temporal evolution of the laser-created plasmas as well as their dependence on incident laser pulse energy has been studied. Specifically, the emission from the two strongest observed hydrogen transitions and specific vibrational band emissions from two molecular transitions in OH and NH were studied to determine the experimental parameters necessary for optimal signal-to-background, signal-to-noise, and total absolute emission intensity. As well, plasma parameters such as the excitation temperature and electron density were calculated from the ratio of hydrogen transition emission intensities and the Stark-broadening of those transitions.

It is apparent that the extreme longevity (out to 40  $\mu$ s) of emission from the hydrogen-containing molecules could provide a sensitive probe of the liquid matrix allowing a measurement to be made at far-extended gate delay times where contributions from background continuum emission and other sources of noise may be eliminated.

## Acknowledgements

The authors would like to thank Prof. Peter Hoffman for the use of the water purification system, Dr. Mohamad Sabsabi for helpful advice on construction of the laser-delivery system, and the Wayne State University Department of Physics and Astronomy (College of Liberal Arts and Sciences) for financial support.

## References

- [1] L.J. Radziemski, D.A. Cremers, *Laser-Induced Plasmas and Applications*, Marcel Dekker, Inc., New York, 1989.
- [2] K. Song, Y.-I. Lee, J. Sneddon, Recent developments in instrumentation for laser-induced breakdown spectroscopy, *Appl. Spectrosc. Rev.* 37 (2002) 89–117.
- [3] E. Tognoni, V. Palleschi, M. Corsi, G. Cristoforetti, Quantitative micro-analysis by laser-induced breakdown spectroscopy: a review of the experimental approaches, *Spectrochim. Acta Part B* 57 (2002) 1115–1130.
- [4] For an example of the variety of applications to which LIBS has been applied see the special edition on laser-induced breakdown spectroscopy, *Appl. Opt.* 42 (2003).
- [5] O. Samek, D.C.S. Beddows, J. Kaiser, S. Kukhlevsky, M. Liska, H.H. Telle, J.J. Young, Application of laser-induced breakdown spectroscopy to in situ analysis of liquid samples, *Opt. Eng.* 39 (2000) 2248–2262.
- [6] T. Kim, Y. Yoon, Laser-induced breakdown spectroscopy for elemental analysis in water, *J. Kor. Phys. Soc.* 37 (2000) 761–765.
- [7] K.M. Lo, N.H. Cheung, ArF laser-induced plasma spectroscopy for part-per-billion analysis of metal ions in aqueous solutions, *Appl. Spectrosc.* 56 (2002) 682–688.
- [8] P. Yaroshchik, R.J.S. Morrison, D. Body, B.L. Chadwick, Quantitative determination of wear metals in engine oils using laser-induced breakdown spectroscopy: a comparison between liquid jets and static liquids, *Spectrochim. Acta Part B* 60 (2005) 986–992.
- [9] S. Koch, W. Garen, M. Muller, W. Neu, Detection of chromium in liquids by laser-induced breakdown spectroscopy (LIBS), *Appl. Phys. A* 79 (2004) 1071–1073.
- [10] A. De Giacomo, M. Dell'aglio, O. De Pascale, Single pulse laser-induced breakdown spectroscopy in aqueous solution, *Appl. Phys. A* 79 (2004) 1035–1038.
- [11] N. Yamaguchi, H. Hotokezaka, S. Nagasaki, S. Tanaka, Direct quantitative analysis of particulate aluminum suspended in water using laser-induced breakdown spectroscopy, *Soil Sci. Plant Nutr.* 51 (2005) 911–916.
- [12] P. Fichet, A. Toussaint, J.-F. Wagner, Laser-induced breakdown spectroscopy: a tool for analysis of different types of liquids, *Appl. Phys. A* 69 (1999) S591–S592.
- [13] P. Fichet, P. Mauchien, J.-F. Wagner, C. Moulin, Quantitative elemental determination in water and oil by laser induced breakdown spectroscopy, *Anal. Chim. Acta* 429 (2001) 269–278.
- [14] A. Kumar, F.Y. Yueh, T. Miller, J.P. Singh, Detection of trace elements in liquids by laser-induced breakdown spectroscopy with a Meinhard nebulizer, *Appl. Opt.* 42 (2003) 6040–6046.
- [15] S. Nakamura, Y. Ito, K. Sone, H. Hiraga, K. Kaneko, Determination of an iron suspension in water by laser-induced breakdown spectroscopy with two sequential laser pulses, *Anal. Chem.* 68 (1996) 2981–2986.
- [16] A.E. Pichahchy, D.A. Cremers, M.J. Ferris, Elemental analysis of metals under water using laser-focused breakdown spectroscopy, *Spectrochim. Acta Part B* 52 (1997) 25–39.
- [17] X.Y. Pu, W.Y. Ma, N.H. Cheung, Sensitive elemental analysis of aqueous colloids by laser-induced plasma spectroscopy, *Appl. Phys. Lett.* 83 (2003) 3416–3418.
- [18] A. Kuwako, Y. Uchida, K. Amaeda, Supersensitive detection of sodium in water with use of dual-pulse laser-induced breakdown spectroscopy, *Appl. Opt.* 42 (2003) 6052–6056.
- [19] S. Koch, R. Court, W. Garen, W. Neu, R. Reuter, Detection of manganese in solution in cavitation bubbles using laser-induced breakdown spectroscopy, *Spectrochim. Acta Part B* 60 (2005) 1230–1235.
- [20] A. De Giacomo, M. Dell'aglio, E. Colao, R. Fantoni, V. Lazic, Double-pulse LIBS in bulk water and on submerged bronze samples, *Appl. Surf. Sci.* 247 (2005) 157–162.
- [21] R.L. Vander Wal, T.M. Tichich, J.R. West Jr., P.A. Householder, Trace metal detection by laser-induced breakdown spectroscopy, *Appl. Spectrosc.* 53 (1999) 1226–1236.
- [22] P. Yaroshchik, R.J.S. Morrison, D. Body, B.L. Chadwick, Quantitative determination of wear metals in engine oils using LIBS: the use of paper substrates and a comparison between single- and double-pulse LIBS, *Spectrochim. Acta Part B* 60 (2005) 1482–1485.
- [23] D.C.S. Beddows, O. Samek, M. Liska, H.H. Telle, Single pulse laser-induced breakdown spectroscopy of samples submerged in water using a single fibre-light delivery system, *Spectrochim. Acta Part B* 57 (2002) 1461–1471.
- [24] V. Lazic, F. Colao, R. Fantoni, V. Spizzicchio, Laser-induced breakdown spectroscopy in water: improvement of the detection threshold by signal processing, *Spectrochim. Acta Part B* 60 (2005) 1002–1013.
- [25] V. Detalle, R. Heon, M. Sabsabi, L. St. -Onge, An evaluation of a commercial Echelle spectrometer with intensified charge-coupled device detector for materials analysis by laser-induced plasma spectroscopy, *Spectrochim. Acta Part B* 56 (2001) 1011–1025.
- [26] P. Fichet, D. Menut, R. Brennetot, E. Vors, A. Rivoallan, Analysis by laser-induced breakdown spectroscopy of complex solids, liquids, and powders with an Echelle spectrometer, *Appl. Opt.* 42 (2003) 6029–6035.
- [27] M. Sabsabi, V. Detalle, M.A. Harith, W. Tawfik, H. Imam, Comparative study of two new commercial Echelle spectrometers equipped with intensified CCD for analysis of laser-induced breakdown spectroscopy, *Appl. Opt.* 42 (2003) 6094–6098.
- [28] B. Charfi, M.A. Harith, Panoramic laser-induced breakdown spectrometry of water, *Spectrochim. Acta Part B* 57 (2002) 1141–1153.
- [29] R.W.B. Pearse, A.G. Gaydon, *The Identification of Molecular Spectra*, Chapman and Hall, London, 1976.
- [30] T.N. Piehler, F.C. DeLucia Jr., C.A. Munson, B.E. Homan, A.W. Miziolek, K.L. McNesby, Temporal evolution of the laser-induced breakdown spectroscopy spectrum of aluminum metal in different bath gases, *Appl. Opt.* 44 (2005) 3654–3660.
- [31] R.J. Nordstrom, Study of laser-induced plasma emission spectra of N<sub>2</sub>, O<sub>2</sub>, and ambient air in the region 350 nm to 950 nm, *Appl. Spectrosc.* 49 (1995) 1490–1499.
- [32] A. Portnov, S. Rosenwaks, I. Bar, Identification of organic compounds in ambient air via a characteristic emission following laser ablation, *J. Lumin.* 102–103 (2003) 408–413.
- [33] A.M. Keszler, L. Nemes, Time averaged emission spectra of Nd:YAG laser induced carbon plasmas, *J. Mol. Struct.* 695–696 (2004) 211–218.
- [34] M. Baudelet, L. Guyon, J. Yu, J.-P. Wolf, T. Amodeo, E. Frejafon, P. Laloi, Spectral signature of native CN bonds for bacterium detection and identification using femtosecond laser-induced breakdown spectroscopy, *Appl. Phys. Lett.* 88 (2006) 063901–1–3.
- [35] N. Glumac, Aluminum nitride emission from a laser-induced plasma in a dispersed aerosol, *J. Appl. Phys.* 98 (2005) 053301–1–6.
- [36] J.B. Simeonsson, A.W. Miziolek, Time resolved emission studies of ArF-laser-produced microplasmas, *Appl. Opt.* 32 (1993) 939–947.
- [37] D.A. Cremers, L.J. Radziemski, Detection of chlorine and fluorine in air by laser-induced breakdown spectrometry, *Anal. Chem.* 55 (1983) 1252–1258.
- [38] M. Sabsabi, P. Cielo, Quantitative analysis of aluminum alloys by laser-induced breakdown spectroscopy and plasma characterization, *Appl. Spectrosc.* 49 (1995) 499–507.
- [39] H.R. Griem, *Plasma Spectroscopy*, McGraw-Hill, New York, 1964.
- [40] A.P. Thorne, *Spectrophysics*, Chapman and Hall, London, 1998.